Chapter 4

Bolocam Survey for 1.1 mm Dust Continuum Emission in the Serpens Molecular Cloud

Abstract

We present the results from a 1.1 mm survey for dust continuum emission of the Serpens molecular cloud, using Bolocam at the CSO. This represents the final survey in a three-cloud study of nearby star-forming molecular clouds. We identify 35 1.1 mm sources a point source detection limit of 0.13 $M_\odot$. Sources are slightly elongated on average, and have a narrow distribution of sizes with a mean of 55″. The average mass of the sample is 2.6 $M_\odot$, and the total mass in 1.1 mm cores is 92 $M_\odot$, accounting for 2.7% of the total cloud mass The differential mass distribution can be fit by a power law with slope $\alpha = 1.6 \pm 0.2$ above 0.35 $M_\odot$. These basic results will be utilized in the next chapter to compare the properties of the core populations of Perseus, Ophiuchus, and Serpens.

4.1 Introduction

We have recently completed 1.1 mm surveys of the Perseus (Enoch et al. 2006; chapter 2) and Ophiuchus molecular clouds (Young et al. 2006; chapter 3) with Bolocam

This chapter is adapted from the first half of Enoch et al. 2007, ApJ, in press.

at the Caltech Submillimeter Observatory (CSO). In this chapter we present a similar 1.1 mm survey of 1.5 deg^2 of the Serpens cloud, completing our three-cloud study of dust continuum emission in nearby northern star-forming molecular clouds. Millimeter maps trace ongoing star formation on large scales by detecting dust emission from dense protostellar envelopes and starless cores. These observations are coordinated to cover the area mapped with *Spitzer* Space Telescope IRAC and MIPS observations of Serpens from the "Cores to Disks" (hereafter c2d; Evans et al., 2003) legacy project.

The Serpens molecular cloud is an active star formation region at a distance of $d = 260 \pm 10$ pc (Straizys, Cernis, & Bartasiute, 1996). Although the cloud extends more then 10 deg^2 as mapped by optical extinction (Cambrésy, 1999), most observations of the region have been focused near the main Serpens cluster at a Right Ascension (RA) of 18^h30^m and declination (Dec) of $1°15'$ (J2000).

The Serpens cluster is a highly extincted region with a high density of young stellar objects (YSOs), including a number of Class 0 protostars. It has been studied extensively at near-infrared, far-infrared, submillimeter, and millimeter wavelengths (e.g., Eiroa & Casali, 1992; Hurt & Barsony, 1996; Larsson et al., 2000; Davis et al., 1999; Casali, Eiroa, Duncan, 1993; Testi & Sargent, 1998). Some recent work has also drawn attention to a less well known cluster to the south, sometimes referred to as Serpens/G3-G6 (Djupvik et al., 2006; Harvey et al., 2006). Beyond these two clusters no continuum millimeter or submillimeter continuum surveys have been done that could shed light on large-scale star formation processes.

In this chapter we briefly present the basic results from the Serpens survey. In the next chapter (chapter 5), we will compare the results from the three clouds to gain a more complete understanding of star formation in molecular clouds. The Bolocam observations and data reduction (§4.2) are described, to the extent that they differ from the detailed information in chapter 2. We then discuss general results such as cloud morphology (§4.3) and source properties (§4.3.2), including the 1.1 mm core mass distribution. We end with a summary in (§4.4).

4.2 Observations and Data Reduction

Observations and data reduction for Serpens follow the same methodology as for Perseus and Ophiuchus. The data reduction techniques we have developed for the Bolocam molecular cloud data are described in detail in chapter 2, including removal of sky noise, construction of pointing and calibration models, application of iterative mapping, and source extraction. Given these previous descriptions, only details specific to Serpens will be presented here. Further information about the Bolocam instrument and reduction pipeline is also available in Laurent et al. (2005).

4.2.1 Observations

As for Perseus and Ophiuchus, millimeter continuum observations of Serpens were made with Bolocam[1] at the CSO on Mauna Kea, Hawaii. The 1.1 mm observations were designed to cover a region with $A_V \geq 6$ mag in the visual extinction map of Cambrésy (1999), shown in figure 4.1. As demonstrated in figure 4.1, this ensures that the Bolocam observations overlap as closely as possible with the region of Serpens observed with *Spitzer* IRAC and MIPS as part of the c2d Legacy project. In practice, the Bolocam survey covers a region slightly larger than the IRAC map, and slightly smaller than the MIPS map.

Serpens was observed during two separate runs in 2003 May 21–June 9 and 2005 June 26–30. During the 2003 run, 94 of the 144 channels were operational, compared to 109 during the 2005 run. Scans of Serpens were made at a rate of $60''$ sec^{-1} with no chopping of the secondary. The final map consists of 13 scans from 2003 in good weather, and 17 scans from 2005 in somewhat poorer conditions. Each scan covered the entire 1.5 deg^2 area and took $35 - 40$ minutes to complete depending on the scan direction. Scans were made in two orthogonal directions, approximately half in RA and half in Dec This strategy allows for good cross-linking in the final map, sub-Nyquist sampling, and minimal striping from $1/f$ noise. Scans were observed in sets of three offset by $-43''$, $0''$, $+43''$ to optimize coverage.

[1] http://www.cso.caltech.edu/bolocam

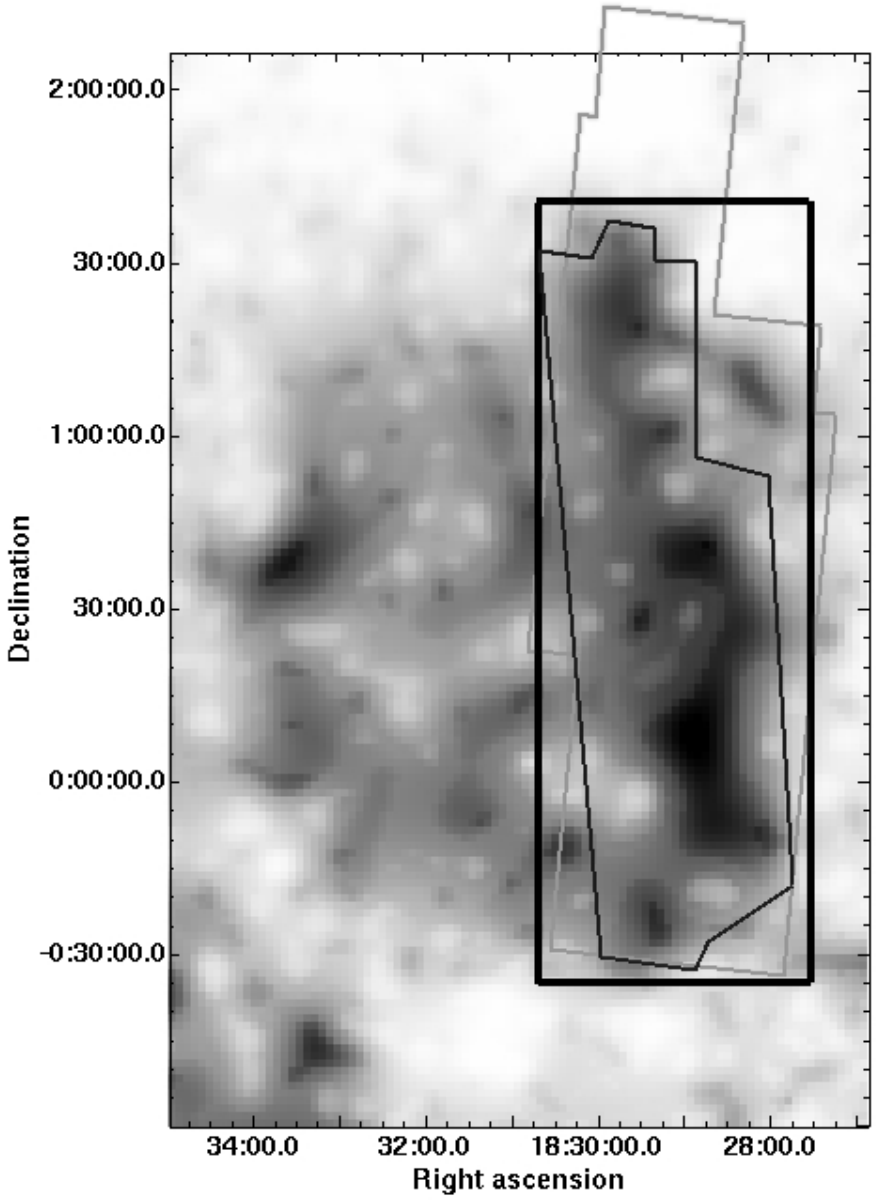

Figure 4.1 Bolocam 1.1 mm (thick line) and Spitzer c2d IRAC (thin line) and MIPS (gray line) coverage of Serpens overlaid on the Cambrésy (1999) visual extinction map. The area observed with IRAC was chosen to cover $A_V \geq 6$ mag in this portion of the cloud. Our Bolocam survey covers the same area as the IRAC and a slightly smaller area than the MIPS observations.

In addition, small maps of pointing sources were observed approximately every 2 hours, and at least one primary flux calibration source, including Neptune, Uranus, and Mars, was observed each night. Several larger beam maps of planets were also made during each run, to characterize the Bolocam beam at 1.1 mm.

4.2.2 Pointing and Flux Calibration

A pointing model for Serpens was generated using two nearby pointing sources, G 34.3 and the quasar 1749+096. After application of the pointing model, a comparison to the literature SCUBA 850 μm positions of four bright known sources (Davis et al., 1999) in the main Serpens cluster indicated a constant positional offset of (δRA, δDec) = ($5''$, $-10''$). We corrected for the positional offset, but estimate an uncertainty in the absolute pointing of $10''$, still small compared to the beam size of $31''$. The relative pointing errors, which cause blurring of sources and an increase in the effective beam size, should be much smaller, approximately $5''$. Relative pointing errors are characterized by the rms pointing uncertainty, derived from the deviations of G 34.3 from the pointing model.

Calibrator maps of Neptune, Uranus, and G 34.3, observed at least once per night, were used to construct a calibration curve for each run. A systematic uncertainty of approximately 10% is associated with the absolute flux calibration, but relative fluxes should be much more accurate.

4.2.3 Cleaning and Mapping

Aggressive sky subtraction techniques are required for Bolocam data to remove sky noise, which dominates over the astronomical signal before cleaning. As in chapter 2, we remove sky noise from the Serpens scans using Principal Component Analysis (PCA) cleaning (Laurent et al. (2005) and references therein), subtracting 3 PCA components. Iterative mapping is necessary to restore source flux lost in the sky subtraction process. Data from the 2003 and 2005 observing runs were iteratively mapped separately because they required different pointing and flux calibration models. After

iterative mapping the two epochs were averaged, weighting by the square root of the observational coverage.

The final 10″ pixel^{-1} Serpens map is shown in figure 4.2, with the well known northern Serpens cluster, Cluster A (Harvey et al., 2006), indicated, as well as the southern cluster, Cluster B (Serpens/G3-G6). Covering a total area of 1.5 deg^2, or 30.9 pc^2 at a distance of 260 pc, the map has a linear resolution of 7.3×10^3 AU.

4.2.4 Source Identification

Observational coverage, which depends on the scan strategy, number of scans, and number of bolometer channels, was very uniform for Serpens; trimming regions where the coverage was less than 30% of the peak coverage was equivalent to cutting off the noisy outer edges of the map. The average coverage in the Serpens map is 1600 hits per pixel, where a hit means a bolometer passed over this position, with variations across the map of 18%. The average coverage corresponds to an integration time of 13 minutes per pixel, although individual pixels are not independent because the map is oversampled.

Sources are identified in the optimally filtered map, using the peak-finding routine described in §2.4.1 and a detection limit of 5 times the local rms noise. We identify 35 sources above the 5σ detection limit, which is typically 50 mJy beam^{-1} The local rms noise per beam is calculated in small ($\sim$ 45 arcmin^2) boxes in the noise map of Serpens, shown in figure 4.3 with the positions of identified sources overlaid. The mean rms noise is 9.5 mJy beam^{-1}, but is higher near bright sources. Most of the 18% variations in the local rms noise occur in the main cluster region, where calculation of the noise is confused by residual artifacts from bright sources. Such artifacts must contribute significantly to noise fluctuations; coverage variations alone would predict rms noise variations of only $\sqrt{18} = 4\%$. This means that faint sources near bright regions have a slightly lower chance of being detected than those in isolation.

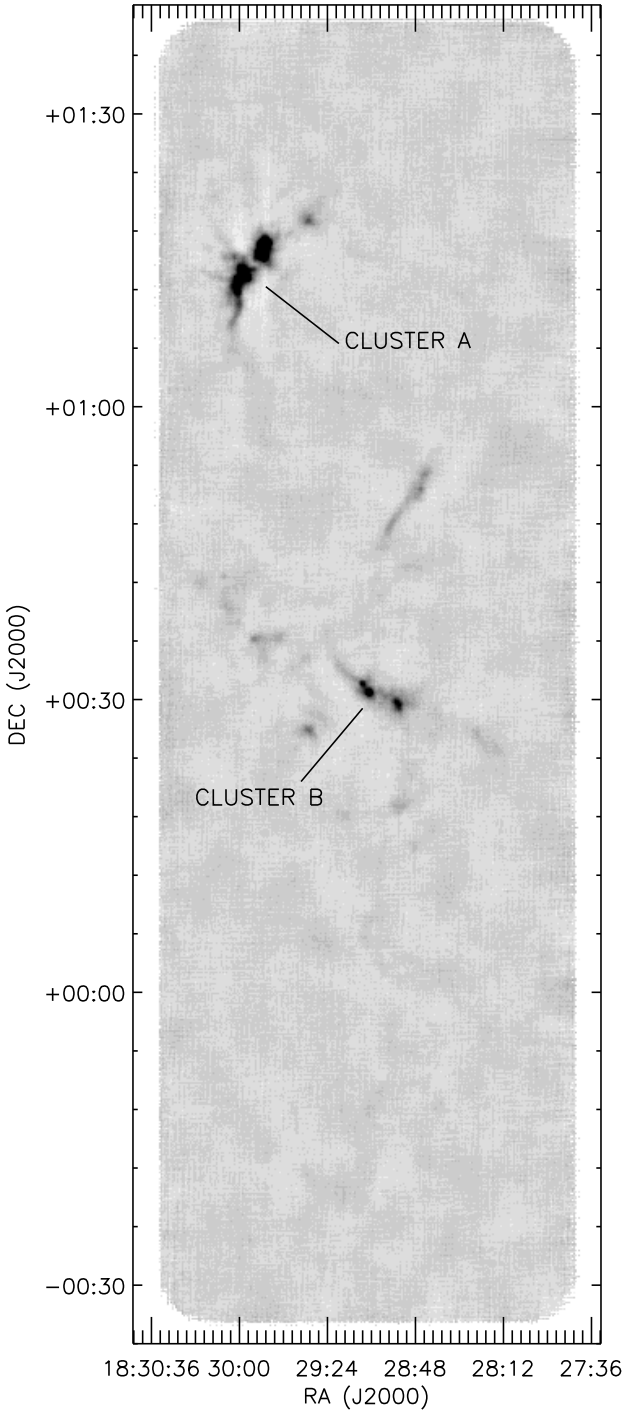

Figure 4.2 Bolocam 1.1 mm map of 1.5 deg^2 (31 pc^2 at d = 260 pc) in the Serpens molecular cloud. Bolocam has a resolution of 31″, and the map is binned to 10″ pixel^{-1}.

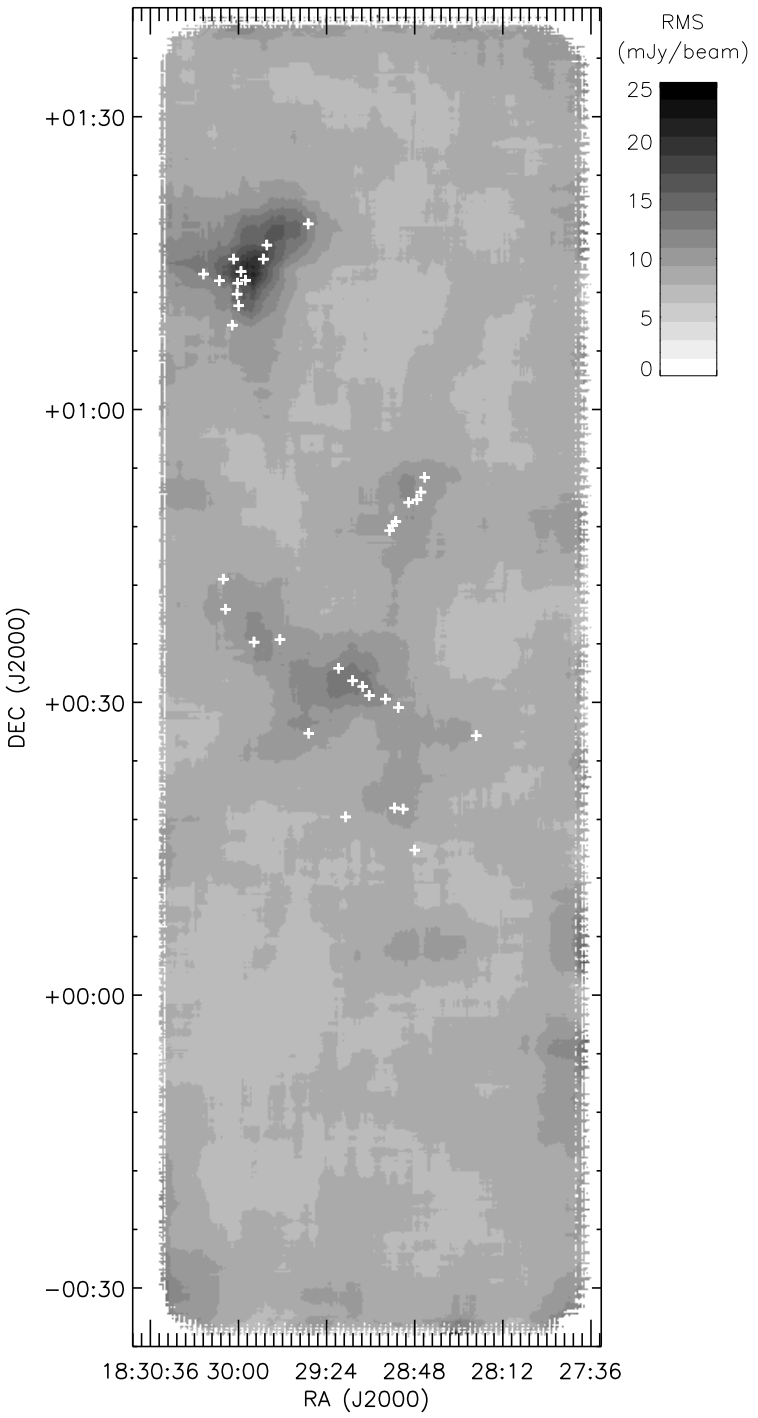

Figure 4.3 Map of the local 1σ rms noise per beam in the Serpens map. Positions of the 35 sources are indicated by white plus symbols. The average rms noise is 9.5 mJy beam^{-1}, varying by 18% across the map. The noise is higher near bright sources due to sky subtraction residuals.

4.3 Results

Positions of the 35 detected sources are listed in table 4.1, and identified by red circles in figure 4.4. Figure 4.4 also shows magnifications of the more densely populated source regions, including Cluster A and Cluster B. We do not see any circularly symmetric extended emission on scales $\gtrsim 3'$ in the map. It should, in principle, be possible to recover symmetric structures up to the array size of $7\farcm5$, but our simulations show that sources $\gtrsim 4'$ in size are severely affected by cleaning and therefore difficult to fully recover with iterative mapping. The map does contain larger filamentary structures up to $8'$ long. In particular, the long filament between Cluster A and Cluster B is reminiscent of the elongated ridge near B1 in Perseus (chapter 2). The Serpens filament does not contain the bright compact sources at either end that are seen in the B1 ridge, however.

Previous millimeter-wavelength maps of Cluster A, such as the 1.1 mm UKT14 map of Casali, Eiroa, & Duncan (1993) and the 850 μm SCUBA map of Davis et al. (1999), generally agree with our results in terms of morphology and source structure. Not all of the individual 850 μm sources are detected by our peak-finding routine, presumably due to the poorer resolution of Bolocam ($30''$) compared to SCUBA ($14''$), but most can, in fact, be identified by eye in the Bolocam map. An IRAM 1.3 mm continuum map of Cluster B with $11''$ resolution (Djupvik et al., 2006) is visually quite similar to our Bolocam map of the region. We detect each of the four 1.3 mm sources identified (MMS1-4), although the 1.3 mm triplet MMS1 is seen as a single extended source in our map.

Most of the brightest cores, in particular those in Cluster A, are associated with known YSOs including a number of Class 0 objects (Hurt & Barsony, 1996; Harvey et al., 2006). All bright 1.1 mm sources are aligned with bright 160 μm emission in the *Spitzer* MIPS map of Serpens observed by the c2d legacy project (Harvey et al., 2007). Fainter millimeter sources are usually associated with extended 160 μm filaments, but do not necessarily correspond to point sources in the MIPS map. Conversely, one bright extended region of 160 μm emission just south of Cluster A contains no 1.1 mm

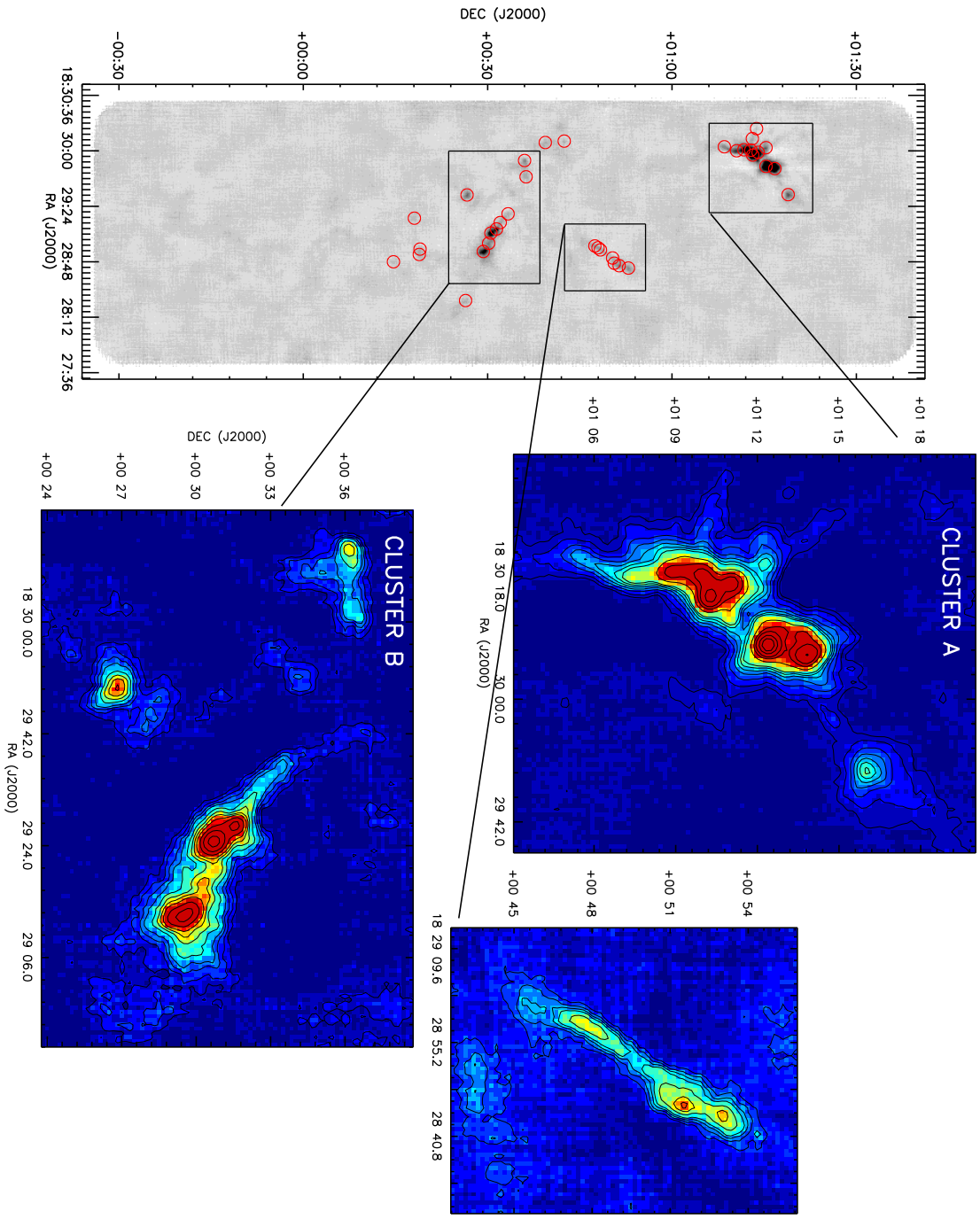

Figure 4.4 Bolocam 1.1 mm map of Serpens with the positions of the 35 sources detected above 5σ indicated by red circles. Inset maps magnify the most densely populated source regions, including the well known northern Cluster A, Cluster B to the south, and an elongated filament reminiscent of the B1 ridge in Perseus (chapter 2). Despite the low rms noise level reached (9.5 mJy beam^{-1}), few sources are seen outside the cluster regions. Many bright 1.1 mm sources are associated with YSOs (Harvey et al., 2006), and all are coincident with 160 μm emission.

sources. This area also exhibits extended emission at 70 and 24 μm, which may be indicative of warmer, more diffuse material than that of the dense cores detected at 1.1 mm.

4.3.1 Comparison to Visual Extinction

Despite the low rms noise level achieved in Serpens, very few sources are seen outside the main clusters; most of the area that we mapped appears devoid of 1.1 mm emission, despite being in a region of high extinction. Figure 4.5 shows a comparison between the Bolocam millimeter map (gray-scale) and visual extinction (contours) derived from c2d near- and mid-infrared Spitzer data.

The majority of sources (90%–95%) detected by IRAC and MIPS in the c2d clouds have spectral energy distributions characteristic of reddened stars. Thus we have measures of the visual extinction for many lines of sight through the molecular clouds imaged by c2d, including Perseus, Ophiuchus, and Serpens. Here we describe the derivation of extinction (A_V) maps that will be used in this and the following chapters.

Line-of-sight extinction values are derived by fitting the R_V=5.5 dust model of Weingartner & Draine (2001) to the near-infrared through mid-infrared SED (Evans et al., 2006). For each of the three clouds, the derived line-of-sight extinctions were convolved with uniformly spaced 90″ Gaussian beams to construct an extinction map. The c2d extinction maps accurately trace column densities up to $A_V \sim 40$ mag, but are relatively insensitive to small regions of high volume density, because they rely on the detection of background stars. Thus the extinction maps are complementary to the 1.1 mm observations, which trace high volume density structures (see §5.3). In figure 4.5, the A_V map for Serpens is smoothed to an effective resolution of 2.′5.

As can be seen in figure 4.5, nearly all Serpens millimeter sources lie within regions of high visual extinction ($A_V \geq 10$ mag) and, in particular, all bright Bolocam sources are associated with areas of $A_V \geq 15$ mag. Nevertheless, there are a number of high extinction areas ($A_V \geq 12$ mag) with no detectable 1.1 mm sources. A similar

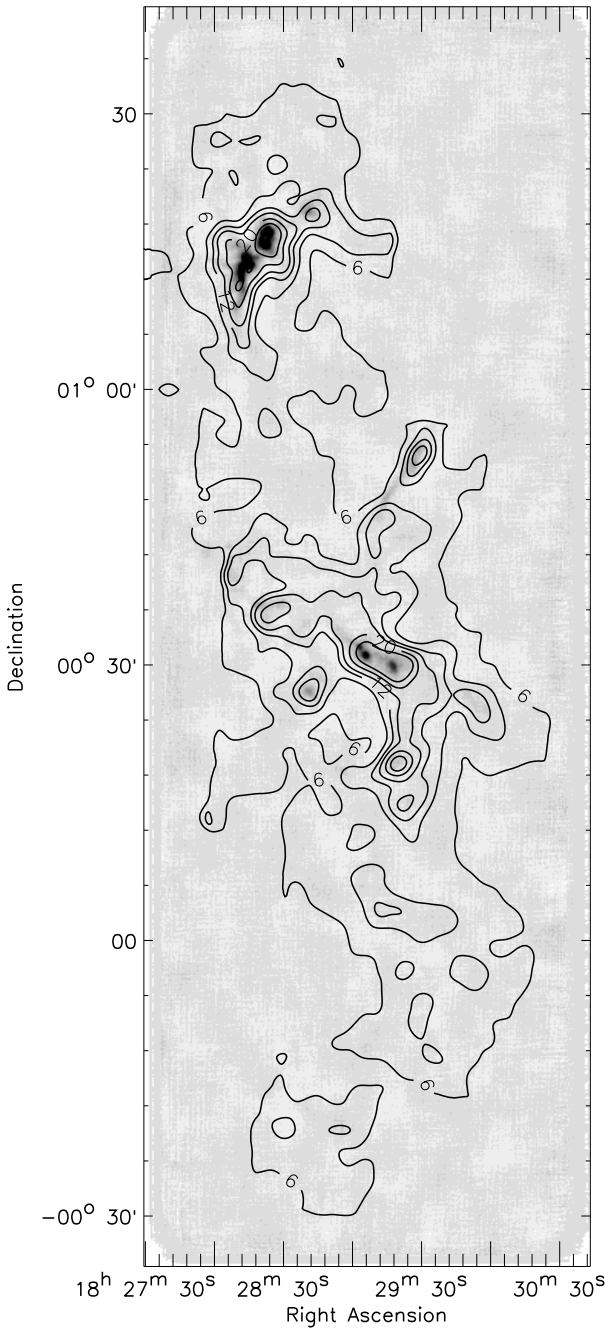

Figure 4.5 Visual extinction (A_V) contours calculated from c2d Spitzer maps, as described in §4.3.2.3, overlaid on the gray-scale 1.1 mm map. Contours are $A_V = 6, 9, 12, 15, 20, 25$ mag and are smoothed to an effective resolution of 2.′5. All bright 1.1 mm cores are found in regions of high (> 15 mag) extinction, but not all high A_V areas are associated with strong millimeter sources.

general trend was noted in both Perseus (chapter 2) and Ophiuchus (chapter 3), with relatively few sources found outside the major groups and clusters associated with the highest extinction. In chapter 5 (§5.5.5) we examines the relationship between A_V and 1.1 mm sources in more detail.

4.3.2 Source Properties

4.3.2.1 Positions and Photometry

Positions, peak flux densities, and signal-to-noise ratio (S/N) for the 35 1.1 mm sources identified in the Bolocam map of Serpens are listed in table 4.1. Table 4.1 also lists the most commonly used name from the literature for known sources, and indicates if the 1.1 mm source is coincident (within 60″) with a MIPS 24 μm source from the c2d database (Harvey et al., 2007). The uncertainty in the peak flux density is the local rms beam^{-1} and does not include an additional 15% systematic uncertainty.

Table 4.2 lists photometry in fixed apertures of diameter 40″, 80″, and 120″, the total integrated flux density. Aperture sizes for the total flux density are limited by the distance to the nearest neighboring source, or 120″, whichever is larger. Uncertainties are based on the local rms noise and the aperture size, and do not include an additional 15% systematic uncertainty.

Table 4.1. Identified sources in Serpens

ID	RA (2000) (h m s)	Dec (2000) ($^\circ$ $'$ $''$)	Peak (mJy/beam)	S/N	other names	MIPS source?
Bolo1	18 28 23.1	+00 26 34.6	95 (12)	5.0		N
Bolo2	18 28 44.0	+00 53 02.8	198 (12)	9.9		N
Bolo3	18 28 45.8	+00 51 32.4	227 (12)	13.7	IRAS 18262+0050	Y
Bolo4	18 28 47.2	+00 50 45.1	145 (10)	7.1		N
Bolo5	18 28 48.3	+00 14 51.5	73 (9)	5.8		N
Bolo6	18 28 50.8	+00 50 28.6	115 (10)	7.3		N
Bolo7	18 28 53.0	+00 19 03.6	119 (11)	5.4		Y
Bolo8	18 28 55.2	+00 29 28.0	617 (13)	30.8	IRAS 18263+0027; MMS1 (1)	Y
Bolo9	18 28 55.9	+00 48 30.3	141 (10)	9.1		N
Bolo10	18 28 56.6	+00 19 10.4	107 (11)	5.7		N
Bolo11	18 28 57.3	+00 48 06.5	162 (11)	10.9		N
Bolo12	18 28 58.4	+00 47 35.7	172 (11)	12.0		N
Bolo13	18 29 00.2	+00 30 19.8	239 (15)	5.5		Y
Bolo14	18 29 07.0	+00 30 41.5	1016 (14)	59.2	IRAS 18265+0028; MMS2 (1)	Y
Bolo15	18 29 09.6	+00 31 36.9	626 (14)	33.0	MMS3 (1)	Y
Bolo16	18 29 13.5	+00 32 12.6	175 (13)	5.8		N
Bolo17	18 29 16.4	+00 18 15.4	82 (8)	6.7	IRAS 18267+0016	Y
Bolo18	18 29 19.3	+00 33 29.1	104 (12)	6.0		N
Bolo19	18 29 31.5	+00 26 49.3	279 (14)	14.8	MMS4 (1)	N
Bolo20	18 29 31.9	+01 19 00.9	337 (13)	18.3		Y
Bolo21	18 29 43.4	+00 36 25.2	129 (11)	7.7		N
Bolo22	18 29 48.8	+01 16 50.6	1694 (16)	80.7	SMM 9 (2); S68N	Y
Bolo23	18 29 50.2	+01 15 24.6	3010 (20)	138	SMM 1 (2); FIRS 1	Y
Bolo24	18 29 53.8	+00 36 10.1	202 (10)	17.2	IRAS 18273+0034	Y
Bolo25	18 29 57.4	+01 13 14.9	1980 (23)	62.7	SMM 4 (2)	Y
Bolo26	18 29 59.2	+01 14 07.4	1331 (19)	43.0	SMM 3 (2)	Y
Bolo27	18 30 00.3	+01 10 37.8	425 (19)	14.5		Y
Bolo28	18 30 00.7	+01 12 56.5	1266 (19)	34.3	SMM 2 (2)	Y
Bolo29	18 30 01.0	+01 11 49.1	979 (19)	33.5	SMM 11 (2)	Y
Bolo30	18 30 02.5	+01 15 24.5	319 (16)	11.3	SMM 8 (2)	Y
Bolo31	18 30 02.8	+01 08 38.3	214 (16)	10.0		Y
Bolo32	18 30 05.7	+00 39 32.2	105 (12)	5.0		Y
Bolo33	18 30 06.4	+00 42 37.0	126 (11)	8.3		Y
Bolo34	18 30 08.2	+01 13 11.5	153 (11)	7.8		N
Bolo35	18 30 14.7	+01 13 52.6	85 (11)	5.6		N

Note. — Numbers in parentheses are 1σ errors. The peak flux density is the peak value per beam in the $10''$ pixel^{-1} unfiltered map (without the optimal filter applied). The uncertainty in the peak flux density is the local rms beam^{-1} and does not include an additional 15% systematic uncertainty from calibration uncertainties and residual errors after iterative mapping. Other names listed are the most common identifications from the literature, and are not meant to be a complete list. A 1.1 mm source is considered coincident with a MIPS source if the position is within $60''$ of a 24 μm source from the c2d catalog (Harvey et al., 2007). References – (1) Djupvik et al. 2006; (2) Casali, Eiroa, & Duncan 1993

Table 4.2. Photometry, masses, sizes, and morphology for sources in Serpens

ID	Flux(40″) (Jy)	Flux(80″) (Jy)	Flux(120″) (Jy)	Total Flux (Jy)	Mass (10K) ($M_\odot$)	Peak A_V (mag)	FWHM (minor,″)	FWHM (major,″)	PA (°)	$\langle n \rangle$ cm^{-3}	Morphology[1]
Bolo1	0.137 (0.016)	···	···	0.25 (0.03)	0.65 (0.07)	8	52 (1.0)	62 (1.2)	55 (8)	1.0×10^5	extended,elongated,weak
Bolo2	0.282 (0.017)	···	···	0.51 (0.03)	1.34 (0.08)	17	51 (0.5)	63 (0.6)	-57 (4)	2.1×10^5	multiple,extended,elongated
Bolo3	0.324 (0.015)	···	···	0.382 (0.019)	1.00 (0.05)	19	43 (0.4)	55 (0.5)	-77 (3)	3.2×10^5	multiple,extended,round
Bolo4	0.226 (0.013)	···	···	0.28 (0.017)	0.73 (0.04)	12	43 (0.5)	55 (0.6)	49 (4)	2.2×10^5	multiple,extended,elongated
Bolo5	0.094 (0.013)	···	···	0.16 (0.02)	0.41 (0.06)	6	50 (1.2)	63 (1.4)	-68 (8)	7×10^4	extended,round,weak
Bolo6	0.172 (0.013)	···	···	0.210 (0.016)	0.55 (0.04)	10	46 (0.6)	62 (0.8)	-40 (3)	1.1×10^5	multiple,extended,elongated
Bolo7	0.162 (0.015)	···	···	0.162 (0.015)	0.42 (0.04)	10	46 (0.8)	57 (0.9)	-30 (7)	1.0×10^5	multiple,extended,elongated
Bolo8	0.933 (0.018)	1.99 (0.04)	···	2.63 (0.04)	6.87 (0.12)	52	62 (0.2)	74 (0.2)	68 (1)	5.2×10^5	multiple,extended,round
Bolo9	···	···	···	0.169 (0.010)	0.44 (0.03)	12	38 (0.5)	61 (0.7)	-58 (2)	1.5×10^5	multiple,extended,elongated
Bolo10	0.146 (0.015)	···	···	0.146 (0.015)	0.38 (0.04)	9	51 (0.8)	54 (0.9)	11 (25)	8×10^4	multiple,extended,elongated
Bolo11	···	···	···	0.199 (0.011)	0.52 (0.03)	14	37 (0.4)	61 (0.7)	-59 (2)	1.8×10^5	multiple,round,
Bolo12	0.246 (0.014)	···	···	0.246 (0.014)	0.64 (0.04)	15	39 (0.4)	58 (0.6)	-65 (2)	2.2×10^5	multiple,extended,elongated
Bolo13	0.36 (0.02)	···	···	0.36 (0.02)	0.94 (0.05)	20	52 (0.5)	59 (0.5)	-78 (6)	1.7×10^5	multiple,extended,round
Bolo14	1.381 (0.019)	···	···	2.16 (0.03)	5.65 (0.09)	86	47 (0.1)	54 (0.1)	-44 (2)	1.5×10^6	multiple,extended,elongated
Bolo15	0.856 (0.018)	···	···	0.856 (0.018)	2.24 (0.05)	53	44 (0.2)	56 (0.2)	-27 (1)	6.5×10^5	multiple,extended,round
Bolo16	0.222 (0.018)	···	···	0.27 (0.02)	0.71 (0.06)	15	42 (0.5)	62 (0.8)	32 (3)	1.8×10^5	multiple,extended,elongated
Bolo17	0.118 (0.011)	0.24 (0.02)	0.4 (0.03)	0.40 (0.03)	1.05 (0.09)	7	80 (1.1)	97 (1.3)	-66 (5)	3×10^4	extended,elongated
Bolo18	0.144 (0.016)	···	···	0.25 (0.03)	0.65 (0.08)	9	48 (0.8)	71 (1.2)	-41 (3)	9×10^4	multiple,extended,elongated,weak
Bolo19	0.41 (0.018)	0.85 (0.04)	1.28 (0.06)	1.28 (0.06)	3.34 (0.14)	24	74 (0.5)	89 (0.6)	-74 (3)	1.3×10^5	extended,elongated
Bolo20	0.494 (0.018)	1.01 (0.04)	1.57 (0.05)	1.57 (0.05)	4.11 (0.14)	29	87 (0.5)	90 (0.5)	9 (11)	1.2×10^5	extended,elongated
Bolo21	0.177 (0.014)	0.38 (0.03)	···	0.38 (0.03)	0.98 (0.07)	11	53 (0.7)	64 (0.8)	47 (6)	1.3×10^5	multiple,extended,elongated
Bolo22	2.32 (0.02)	···	···	3.78 (0.04)	9.86 (0.10)	144	47 (0.1)	57 (0.1)	73 (1)	2.3×10^6	multiple,extended,round
Bolo23	3.8 (0.03)	5.91 (0.05)	···	5.91 (0.05)	15.44 (0.14)	256	46 (0.1)	47 (0.1)	39 (4)	6.1×10^6	multiple,extended,round

Table 4.2 (cont'd)

ID	Flux(40″) (Jy)	Flux(80″) (Jy)	Flux(120″) (Jy)	Total Flux (Jy)	Mass (10K) ($M_\odot$)	Peak A_V (mag)	FWHM (minor,″)	FWHM (major,″)	PA (°)	$\langle n \rangle$ cm^{-3}	Morphology[1]
Bolo24	0.291 (0.014)	···	···	0.40 (0.02)	1.04 (0.05)	17	46 (0.4)	55 (0.5)	-12 (4)	2.9×10^5	multiple,extended,elongated
Bolo25	2.75 (0.03)	···	···	3.19 (0.04)	8.33 (0.10)	168	44 (0.1)	51 (0.1)	79 (1)	2.9×10^6	multiple,extended,round
Bolo26	1.9 (0.03)	···	···	1.90 (0.03)	4.95 (0.07)	113	48 (0.1)	59 (0.1)	-21 (1)	1.0×10^6	multiple,extended,round
Bolo27	0.65 (0.03)	···	···	1.18 (0.05)	3.09 (0.12)	36	47 (0.3)	69 (0.4)	89 (1)	4.6×10^5	multiple,extended,elongated
Bolo28	1.9 (0.03)	···	···	1.90 (0.03)	4.96 (0.06)	108	48 (0.1)	59 (0.1)	-47 (1)	1.0×10^6	multiple,extended,round
Bolo29	1.41 (0.03)	···	···	2.44 (0.05)	6.37 (0.12)	83	47 (0.1)	59 (0.2)	-86 (1)	1.4×10^6	multiple,extended,round
Bolo30	0.43 (0.02)	···	···	0.43 (0.02)	1.13 (0.06)	27	48 (0.4)	55 (0.5)	33 (5)	2.6×10^5	multiple,extended,elongated
Bolo31	0.32 (0.02)	0.65 (0.04)	···	0.65 (0.04)	1.70 (0.11)	18	45 (0.5)	74 (0.8)	-65 (2)	2.4×10^5	multiple,extended,elongated
Bolo32	0.151 (0.016)	0.34 (0.03)	···	0.34 (0.03)	0.88 (0.08)	9	57 (0.9)	74 (1.2)	50 (5)	8×10^4	extended,elongated
Bolo33	0.12 (0.015)	···	···	0.128 (0.019)	0.34 (0.05)	11	35 (0.9)	39 (1.1)	25 (17)	6.9×10^6	round
Bolo34	0.181 (0.015)	···	···	0.216 (0.019)	0.56 (0.05)	13	40 (0.6)	60 (0.9)	-70 (3)	1.7×10^5	multiple,extended,elongated
Bolo35	···	···	···	0.06 (0.011)	0.16 (0.03)	7	24 (1.1)	61 (2.9)	-69 (4)	2.4×10^5	multiple,weak

Note. — Masses are calculated according to equation (2.3) from the total flux density assuming a single dust temperature of $T_D = 10$ K and a dust opacity at 1.1mm of $\kappa_{1.1mm} = 0.0114$ cm^{2}g^{-1}. Peak A_V is calculated from the peak flux density as in equation (2.2). FWHM and PAs are from an elliptical Gaussian fit; the PA of the major axis is measured in degrees east of north. $\langle n \rangle$ is the mean particle density as calculated from the total mass and the deconvolved average FWHM size. Numbers in parentheses are 1σ uncertainties. Uncertainties for masses are from photometry only, and do not include uncertainties from κ, T_D, or d, which can be up to a factor of a few or more. Uncertainties for the FWHM and PA are formal fitting errors from the elliptical gaussian fit; additional uncertainties of $10\% - 15\%$ apply to the FWHM, and $\sim 5°$ to the PA (determined from simulations).

[1]The morphology keywords given indicates whether the source is multiple (within $3'$ of another source), extended (major axis FW at $2\sigma > 1'$), elongated (axis ratio at $4\sigma > 1.2$), round (axis ratio at $4\sigma < 1.2$), or weak (peak flux density less than 5 times the rms pixel^{-1} in the unfiltered map).

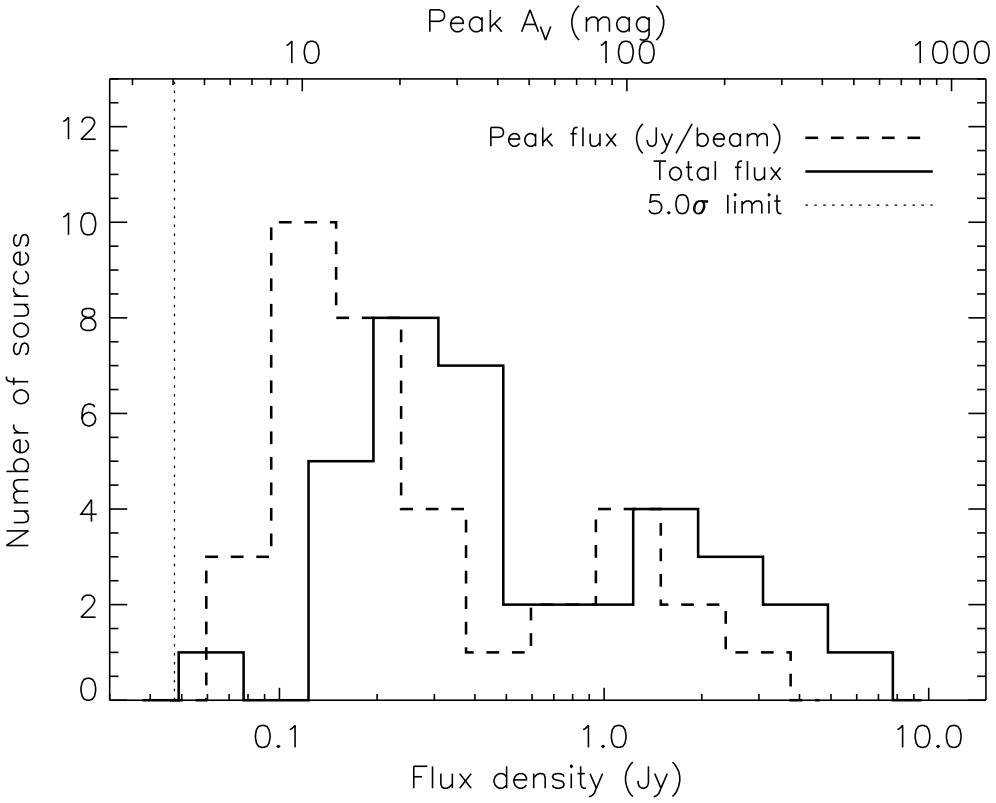

Figure 4.6 Distribution of peak (dashed line) and total (solid line) flux densities of the 35 1.1 mm sources in Serpens. Peak A_V values derived from the 1.1 mm peak flux densities using equation (2.2) are shown on the upper axis. The mean peak flux density of the sample is 0.5 Jy beam^{-1}, the mean peak A_V is 40 mag, and the mean total flux density is 1.0 Jy. The 5σ detection limit of 0.05 Jy (dotted line) is relatively uniform across the cloud.

Peak and total flux density distributions for the 35 1.1 mm sources in Serpens are shown in figure 4.6, with the 5σ detection limit indicated. In general, source total flux densities are larger than peak flux densities because most sources in the map are extended, with sizes larger than the beam. Both distributions look bimodal; all of the sources in the brighter peak are in either Cluster A or Cluster B. The mean peak flux density of the sample is 0.5 Jy beam^{-1}, and the mean total flux density is 1.0 Jy, both with large standard deviations of order the mean value. Peak A_V values of the cores, calculated from the peak flux density as in equation (2.2), are indicated on the upper axis.

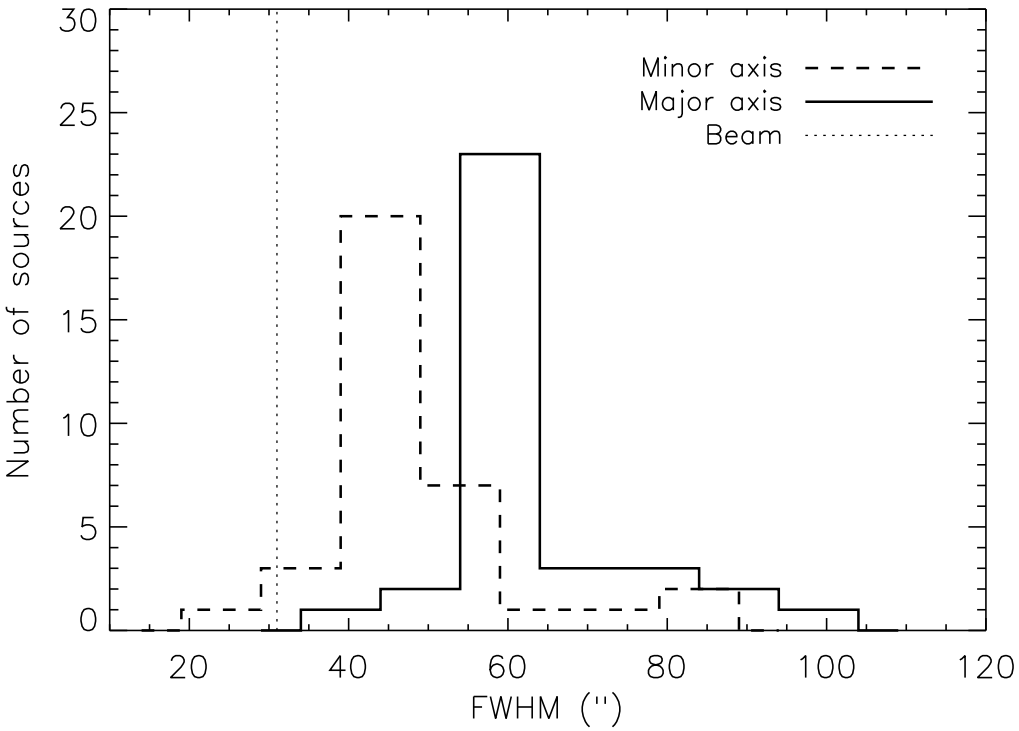

Figure 4.7 Distribution of source FWHM minor axis (dashed line) and major axis (solid line) sizes, determined by an elliptical Gaussian fit. The mean FWHM sizes are 49″ (minor axis) and 63″ (major axis), and the mean axis ratio (major/minor) is 1.3.

4.3.2.2 Sizes and Shapes

Source FWHM sizes and position angles (PA, measured east of north) are measured by fitting an elliptical Gaussian after masking out nearby sources. The best fit major and minor axis sizes and PAs are listed in table 4.2. As can be seen in figure 4.7, the minor axis FWHM values are fairly narrowly distributed around the sample mean of 49″, with a standard deviation of 12″. The major axis FWHM have a similarly narrow distribution with a mean of 63″ and a scatter of 12″. On average sources are slightly elongated, with a mean axis ratio at the half-max contour (major axis FWHM / minor axis FWHM) of 1.3.

A morphology keyword for each source is also given in table 4.2, to describe the general source shape and environment. The majority (28/35) of sources are multiple

(within 3′ of another source), and nearly all (32/35) are extended at the 2σ contour (major axis $> 1'$).

4.3.2.3 Masses, Densities, and Extinctions

Masses listed in table 4.2 calculated as described in §2.5.2 are listed in table 4.2 for the 35 detected sources. A dust temperature of $T_D = 10$ K is assumed for all sources, and a dust opacity of $\kappa_{1.1mm} = 0.0114$ cm^2 g^{-1}, which has been found to be the best fit in a number of radiative transfer models (Evans et al., 2001; Shirley et al., 2002; Young et al., 2003). Uncertainties listed are from the uncertainty in the total flux density only; additional uncertainties from κ, T_D, and d together introduce a total uncertainty in the mass of up to a factor of 4 or more. The total mass in 1.1 mm cores is 92 M$_\odot$, which is only 2.7% of the total cloud mass (3470 M$_\odot$). The cloud mass is estimated from the c2d visual extinction map using $N(\mathrm{H_2})/A_V = 0.94 \times 10^{21}$ mag cm^{-2} (Bohlin, Savage, & Drake, 1978) (see also chapter 5).

Figure 4.8 shows the differential mass function of all 1.1 mm sources in Serpens. The point source detection limit of $0.13 M_\odot$ is indicated, as well as the 50% completeness limit for sources of FWHM 55″ ($0.35 M_\odot$), which is the average size of the sample. Completeness is determined from Monte Carlo simulations of simulated sources inserted into the raw data and run through the reduction pipeline, as described in chapter 2. The best fit power law slope to $dN/dM \propto M^{-\alpha}$ is shown ($\alpha = 1.6$), as well as the best fit lognormal slope ($\sigma = 0.7$, $M_0 = 1.1\ M_\odot$).

Our mass distribution has a flatter slope than that found by Testi & Sargent (1998) from higher resolution (5″) OVRO observations ($\alpha = -2.1$ for $M > 0.35$ M$_\odot$). This may be due in part to the fact that most of our detections, at least 25/35, lie outside the 5.′5 × 5.′5 area observed by Testi & Sargent (1998). The resolution differences of the observations may also contribute significantly; for example, a number of our bright sources break down into multiple objects in the 5″ resolution map.

We calculate peak extinction values for each source from the peak flux density per beam; these peak A_V values are listed in table 4.2, and are also shown on the upper axis of figure 4.6. The average peak A_V of the sample is 41 mag with a

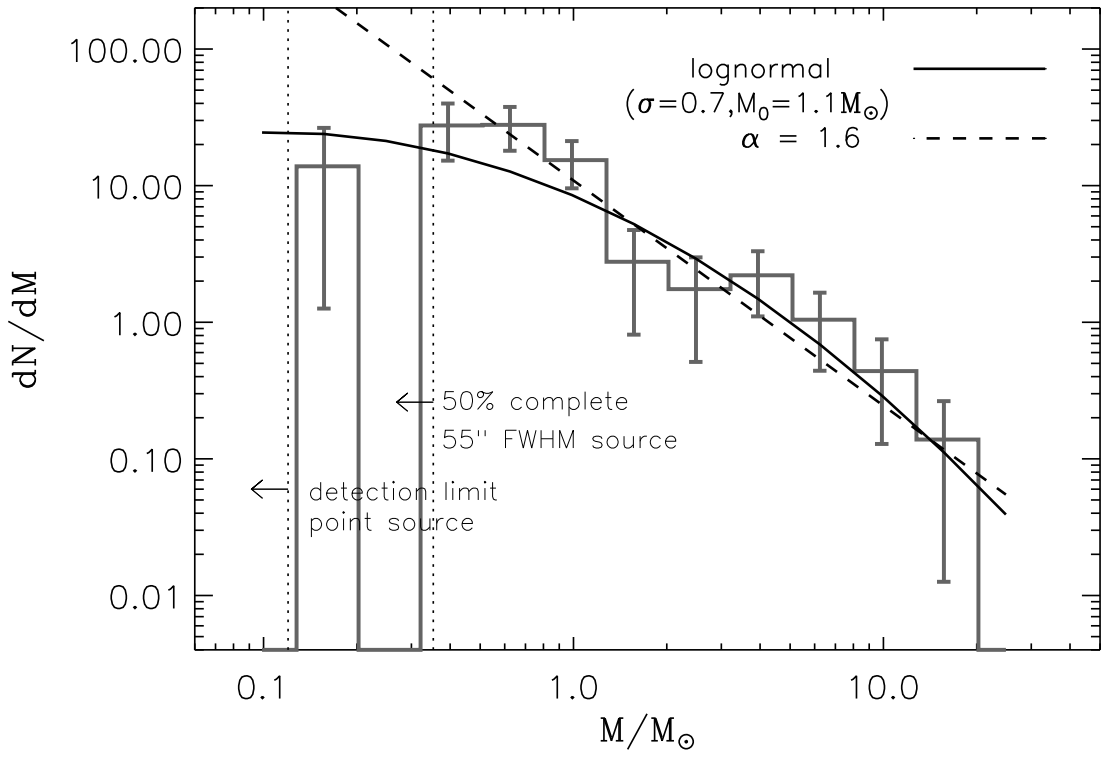

Figure 4.8 Differential mass distribution of the 35 detected 1.1 mm sources in Serpens for masses calculated with $T_D = 10$ K. Dotted lines indicate the point source detection limit and the empirically derived 50% completeness limit for sources with the average FWHM size of 55″. The best fit power law ($\alpha = 1.6 \pm 0.2$) is shown, as well as the best fit lognormal function.

large standard deviation of 55 mag and a maximum A_V of 256 mag. Extinctions calculated from the millimeter emission are generally higher than those from the c2d visual extinction map by approximately a factor of 7, likely a combination of both the higher resolution of the Bolocam map (30″ compared with 90″) and the fact that the extinction map cannot trace the highest volume densities because it relies on the detection of background sources. Grain growth in dense cores beyond that included in the dust opacity from Ossenkopf & Henning (1994) could also lead to an overestimate of the A_V from out 1.1 mm data.

Also listed in table 4.2 is the mean particle density: $\langle n \rangle = 3M/(4\pi R^3 m_H \mu_p)$, where M is the total mass, R is the linear deconvolved radius at half-max, and $\mu_p = 2.33$ is the mean molecular weight per particle. The median of the source mean densities is 2.3×10^5 cm^{-3}, with values ranging from 3.1×10^4 to 6.1×10^6 cm^{-3}.

4.4 Summary

We have completed a 1.1 mm dust continuum survey of Serpens, covering 1.5 deg^2, with Bolocam at the CSO. We identify 35 1.1 mm sources in Serpens above the 5σ detection limit, which is 50 mJy beam^{-1}, or 0.13 M$_\odot$, on average. The sample has an average mass of 2.6 M$_\odot$, and an average source FWHM size of 55″. On average, sources are slightly elongated with a mean axis ratio at half-max of 1.3. The differential mass distribution of all 35 cores is consistent with a power law of slope $\alpha = 1.6 \pm 0.2$ above 0.35 M$_\odot$. The total mass in dense 1.1 mm cores in Serpens is 92 M$_\odot$, accounting for 2.7% of the total cloud mass, as estimated from our c2d visual extinction map.

This work represents the third in a series of three surveys for millimeter continuum emission in nearby star-forming molecular clouds. In chapters 2–4 we have presented the basic results from large-scale mapping of Perseus, Ophiuchus, and Serpens. In the next chapter, we will compare the 1.1 mm source populations in each cloud to infer the effects of environment on dense star-forming cores, and implications for physical conditions in molecular clouds.

Acknowledgments

The authors thank members of the Bolocam team for instrumental and software support, including James Aguirre, Jack Sayers, Glenn Laurent, and Sunil Golwala. Support for this work, part of the Spitzer Legacy Science Program, was provided by NASA through contracts 1224608 and 1230782 issued by the Jet Propulsion Laboratory, California Institute of Technology, under NASA contract 1407. Bolocam was built and commissioned under grants NSF/AST-9618798 and NSF/AST-0098737. KEY was supported by NASA under Grant NGT5-50401, issued through the Office of Space Science. Additional support came from NASA Origins grant NNG04GG24G to NJE and NSF grant AST 02-06158 to JG. MLE acknowledges support of a Moore Fellowship and an NSF Graduate Research Fellowship.

Bibliography

Bohlin, R. C., Savage, B. D., & Drake, J. F. 1978, ApJ, 224, 132

Cambrésy, L. 1999, A&A, 345, 965

Casali, M. M., Eiroa, C., & Duncan, W. D. 1993, A&A, 275, 195

Davis, C. J., Matthews, H. E., Ray, T. P., Dent, W. R. F., & Richer, J. S. 1999, MNRAS, 309, 141

Djupvik, A. A., André, Ph., Bontemps, S., Motte, F., Olofsson, G., Gålfalk, M., & Florén, H.-G. 2006, A&A, 485, 789

Eiroa, C. & Casali, M. M.. 1992, A&A, 262, 468

Enoch, M. L., Young, K. E., Glenn, J., Evans, N. J., II, Golwala, S., Sargent, A. I., Harvey, P., et al. 2006, ApJ, 638, 293

Evans, N. J., II, Allen, L. E., Blake, G. A., Boogert, A. C. A., Bourke, T., Harvey, P. M., Kessler, J. E., et al. 2003, PASP, 115, 965

Evans, N. J., II, Rawlings, J. M. C., Shirley, Y. L., & Mundy, L. G. 2001, ApJ, 557, 193

Evans, N. J., II, et al. 2006, Final Delivery of Data from the c2d Legacy Project: IRAC and MIPS (Pasadena: Caltech), http://data.spitzer.caltech.edu

Harvey, P. M., Chapman, N., Lai, S.-P.. Evans, N. J., II, Allen, L. E., Jørgensen, J. K., Mundy, L. G., et al. 2006, ApJ, 644, 307

Harvey, P. M., Rebull, L. M., Brooke, T., Spiesman, W. J., Chapman, N., Huard, T. L., Evans, N. J., II, et al. 2007, ApJ, in press (preprint: arXiv:0704.0253 [astro-ph])

Hurt, R. L., & Barsony, M. 1996, ApJ, 460, L45

Larsson, B., Liseau, R., Men'shchikov, A. B., Olofsson, G., Caux, E., Ceccarelli, C., Lorenzetti, D., et al. 2000 A&A, 363, 253

Laurent, G., Aguirre, J. E., Glenn, J., Ade, P. A. R., Bock, J. J., Edgington, S. F., Goldin, A., et al. 2005, ApJ, 623, 742

Ossenkopf, V., & Henning, Th. 1994, A&A, 291, 943

Shirley, Y. L., Evans, N. J., II, & Rawlings, J. M. C. 2002, ApJ, 575, 337

Straizys, V., Cernis, K., & Bartasiute, S. 1996, Baltic Astronomy, 5, 125

Testi, L. & Sargent, A. I. 1998, ApJ, 508, L91

Weingartner, J. C. & Draine, B. T. 2001, ApJ, 548, 296

Young, C. H., Shirley, Y. L., Evans, N. J., II, & Rawlings, J. M. C. 2003, ApJS, 145, 111

Young, K. E., Enoch, M. L., Evans, N. J., II, Glenn, J., Sargent, A., Huard, T. L., Aguirre, J., et al. 2006, ApJ, 644, 326